Inverse single-site Fe1(OH)X/Pt(111) model catalyst for preferential oxidation of CO in H2

Chunlei Wang, Heloise Tissot, Markus Soldemo, Junling Lu, Jonas Weissenrieder

Nano Research

ISSN 1998-0124 CN 11-5974/O4
https://doi.org/10.1007/s12274-021-3551-4

Research Article

Inverse single-site $Fe_1(OH)_X$/Pt(111) model catalyst for preferential oxidation of CO in H_2

Chunlei Wang[1], Heloise Tissot[1], Markus Soldemo[2], Junling Lu[3], and Jonas Weissenrieder[1] (✉)

[1] *Materials and Nano Physics, School of Engineering Sciences, KTH Royal Institute of Technology, Stockholm SE-100 44, Sweden*
[2] *Department of Engineering and Physics, Karlstad University, Karlstad SE-651 88, Sweden*
[3] *Department of Chemical Physics, Hefei National Laboratory for Physical Sciences at the Microscale, Key Laboratory of Surface and Interface Chemistry and Energy Catalysis of Anhui Higher Education Institutes, University of Science and Technology of China, Hefei 230026, China*

Received: 3 February 2021 / **Revised:** 17 April 2021 / **Accepted:** 28 April 2021

ABSTRACT

Inverse oxide/metal model systems are frequently used to investigate catalytic structure–function relationships at an atomic level. By means of a novel atomic layer deposition process, growth of single-site Fe_1O_x on a Pt(111) single crystal surface was achieved, as confirmed by scanning tunneling microscopy (STM). The redox properties of the catalyst were characterized by synchrotron radiation based ambient pressure X-ray photoelectron spectroscopy (AP-XPS). After calcination treatment at 373 K in 1 mbar O_2, the chemical state of the catalyst was determined as Fe^{3+}. Reduction in 1 mbar H_2 at 373 K demonstrates a facile reduction to Fe^{2+} and complete hydroxylation at significantly lower temperatures than what has been reported for iron oxide nanoparticles. At reaction conditions relevant for preferential oxidation of CO in H_2 (PROX), the catalyst exhibits a Fe^{3+} state (ferric hydroxide) at 298 K while re-oxidation of iron oxide clusters does not occur under the same condition. CO oxidation proceeds on the single-site $Fe_1(OH)_3$ through a mechanism including the loss of hydroxyl groups in the temperature range of 373 to 473 K, but no reaction is observed on iron oxide clusters. The results highlight the high flexibility of the single iron atom catalyst in switching oxidation states, not observed for iron oxide nanoparticles under similar reaction conditions, which may indicate a higher intrinsic activity of such single interfacial sites than the conventional metal-oxide interfaces. In summary, our findings of the redox properties on inverse single-site iron oxide model catalyst may provide new insights into applied Fe-Pt catalysis.

KEYWORDS

inverse single-site model catalyst, Fe_1O_x/Pt(111), PROX, atomic layer deposition, synchrotron radiation AP-XPS, STM

1 Introduction

Supported nanoparticle catalysts have immense societal impact due to their critical role for heterogeneous catalysts in industrial chemical production [1, 2]. Despite significant progress over the last century, a fundamental understanding of the processes underpinning heterogeneous catalysis is still lacking. It is generally recognized that the metal to metal oxide interface plays a critical role for the activity and selectivity in many reactions [3–10]. However, the nature of the interfacial sites remains elusive. Electronic and geometric properties [11], oxygen defects [12], and interfacial hydroxylation [5] may all greatly influence the catalytic properties. The failure to accurately predict catalytic structure–function relationships is closely tied to the material complexity of applied heterogeneous catalysts that hamper extraction of atomic level information. The situation is further complicated by the dynamic interaction of the catalyst with a reactive environment. To obtain relevant information on the properties of the active phase of catalysts, analysis is preferably conducted at conditions pertinent for the reactions of study [13–15]. A successful strategy for achieving atomic level understanding of catalysts is the application of simplified model catalysts with uniform and well-defined surface structures [8, 16]. This has been proven especially successful when combined with surface sensitive *in-situ* techniques [17, 18]. A widely used model system is the so called inverse oxide/metal catalyst that consists of a metal oxide deposited on a well-defined single crystal metal surface. Inverse catalysts have been employed in studies of structure–function relationships by advanced techniques including scanning tunneling microscopy (STM), X-ray photoemission spectroscopy (XPS), low energy electron diffraction (LEED), and more recently by *in-situ* and ambient pressure surface techniques such as ambient pressure XPS (AP-XPS) [17–21].

Growth of surface oxides with thin film, cluster, or nanoparticle morphologies may be realized through physical vapor deposition (PVD) of the metal and subsequent annealing in O_2 [15, 22]. By controlling the metal coverage and annealing temperature the oxide/metal interface morphology and electronic structure can be tuned to optimize its catalytic activity [23]. Nano dimensional islands of FeO_x deposited on Pt(111) has been extensively studied and the size and structure of the islands show pronounced effects on the reactivity for several reactions [1, 24–27]. However, formation of atomically dispersed iron oxide species supported on Pt(111), the structurally most simple inverse model catalyst, by conventional PVD methods remains challenging.

Recently, Cao et al. demonstrated successful fabrication of

Address correspondence to jonas@kth.se

atomically dispersed iron hydroxide [$Fe_1(OH)_x$] species on silica supported Pt nanoparticles by taking advantage of the self-limiting growth and steric hindrance processes inherent to atomic layer deposition (ALD). The resulting $Fe_1(OH)_x$-Pt powder catalyst exhibits exceptional activity and selectivity for preferential oxidation of CO in a hydrogen ambient (PROX) [28]. Through application of a similar ALD growth method, we here demonstrate the formation of atomically dispersed iron oxide (Fe_1O_x) sites on a Pt(111) surface as shown in the schematic model in Fig. 1. The chemical state and morphology of the model catalyst was investigated *in situ* by STM and AP-XPS at different synthesis steps of the fabrication, confirming the formation of single iron atom species on the Pt surface. The dynamic interplay of the catalytic active sites under PROX conditions was investigated by AP-XPS. The results indicate that the high catalytic efficiency can be traced from the unusually high flexibility in changing the oxidation state of the iron center.

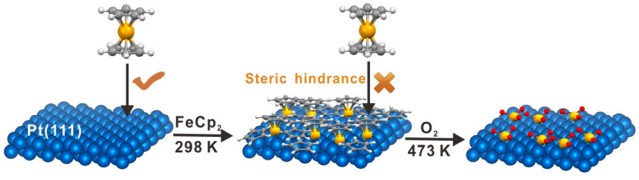

Figure 1 Schematic model of the ALD process that results in atomically dispersed iron oxide species on the Pt(111) surface. Steric hindrance of the precursor Cp ligands ensures separation of FeCp* species and limits the coverage of $FeCp_2$ adsorbed on the Pt(111) surface.

2 Experimental section

The Pt(111) single crystal was cleaned by cycles of Ar^+ sputtering and annealing in 1×10^{-6} mbar O_2 at 873 K followed by annealing in ultrahigh vacuum (UHV) at 973 K. The cleanliness of the surface was confirmed by STM and XPS. The STM images from the clean Pt(111) surface are presented in Fig. S1 in the Electronic Supplementary Material (ESM). Iron oxide clusters were grown *in-situ* on the clean Pt(111) surface using ALD. Pt(111) was first exposed to ferrocene (Alfa Aesar, 99%, the precursor was purified by annealing to 373 K under vacuum for a few cycles) at 298 K and then to 1×10^{-6} mbar of O_2 (99,9995 vol.%) at 473 K in order to remove residual ligands from the precursor [29]. The $FeCp_2$ was introduced into the UHV chamber through a high precision leak valve. Three doses were evaluated: 15 L, 45 L and 500 L (the latter corresponds to a saturation dose, where 1 L = 1 Langmuir). After preparation, the sample was transferred to an Omicron variable temperature STM (VT-STM) operated at 298 K in the constant current imaging mode using electrochemically etched tungsten tips.

The *in-situ* XPS was performed at the AP-XPS endstation of the HIPPIE beamline at the MAX IV laboratory in Lund, Sweden. The endstation consists of an analysis chamber equipped with a differentially pumped Scienta-Omicron HiPP-3 electron energy analyzer. An ambient pressure cell (AP Cell) was docked to the analyzer for the ambient pressure experiments. The Pt(111) sample was cleaned in the preparation chamber of the endstation using the same procedure as previously described. Immediately following ALD preparation, the sample was transferred to the AP Cell and the XP spectra of the C 1s, O 1s, Fe 2p regions were collected at photon energies of 750 and 900 eV. The sample was annealed in 1 mbar O_2, and then in 1 mbar H_2. Finally, 1 mbar of PROX gas with a molar ratio of H_2:CO:O_2 = 4:2:1 was introduced into the cell for analysis under relevant reaction conditions.

3 Results and discussion

The adsorption mechanism for ferrocene on Pt(111) was investigated by STM at increasing coverages. Figure 2 shows the surface after exposure to a dose of 15 L $FeCp_2$ at 298 K. A uniform distribution of well-separated protrusions, assigned to adsorbed $FeCp_2$ fragments, is observed (additional STM images are provided in Fig. S2 in the ESM). Line profile analysis (Fig. 2(c)) shows two types of protrusions with apparent heights of ~ 0.20 and ~ 0.11 nm. In agreement with literature, we assign these protrusions to adsorbed FeCp* and cyclopentadienyl (Cp*) species [30]. The geometric height of a molecularly adsorbed ferrocene is 0.33 nm [31]. No protrusions of such height are observed in the STM images. Taken together, the STM results suggest dissociative adsorption as the preferred reaction pathway. This observation is in agreement with the study by Paul et al. [32]. An interesting observation is that neither islands nor molecular clusters are observed in the STM images at this low coverage.

In conventional ALD processing, the substrate is exposed to a saturating dose of a precursor and then to a reagent for selective removal of the ligands [33]. In the procedure presented here, the precursor ($FeCp_2$) exposure was varied from below saturation to saturation doses. Figure 3 shows STM images from the Pt(111) surface after adsorption of 15 L ferrocene followed by annealing in 1×10^{-6} mbar O_2 at 473 K. The annealing in O_2 removes Cp ligands and oxidizes the Fe atoms deposited onto the surface. The STM analysis shows how the oxidation process reduces the coverage of protrusions on the surface. Desorption of Cp* fragments is expected to reduce the density of protrusions by a factor of 2. However, we observe a significantly larger decrease in coverage. We attribute this excess reduction in coverage to ferrocene recombination and desorption during the annealing process. Figure 3(c) shows a line profile across two typical protrusions. The protrusions are well-separated and exhibit an apparent height of ~ 0.14 nm, similar to the ~ 0.15 nm height observed for a single monolayer iron oxide grown on Pt(111) surfaces [32, 34–37]. The protrusions are uniformly dispersed over the surface, with no apparent formation of islands and only few clusters or nanoparticles observed. The full width at half maximum in the lateral directions of an individual protrusion is ~ 0.6 nm, a similar size to what has been reported for oxidized single atoms of Au and Co supported on copper crystals [38, 39]. The protrusions exhibit symmetrical round shapes suggesting species containing a single oxidized iron atom.

Figure 4 shows a STM image obtained after a dose of 45 L $FeCp_2$ at 298 K followed by an oxygen treatment at 1×10^{-6} mbar and 473 K. The coverage of protrusions with a size and shape corresponding to isolated iron oxide species increases compared to the 15 L dose. Most of the protrusions are isolated, but a slight agglomeration into clusters can now also be observed.

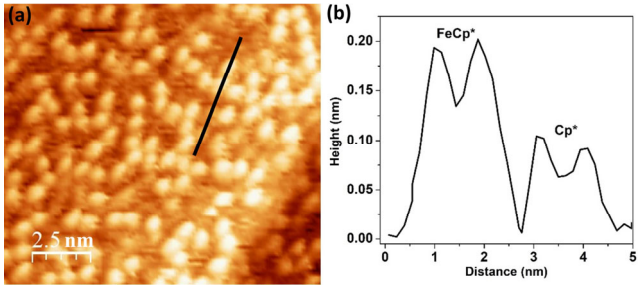

Figure 2 (a) STM images of the Pt(111) surface after exposure to 15 L $FeCp_2$ at 298 K. The STM scanning parameters are −0.32 V and 0.31 nA. (b) height profile across $FeCp_2$ fragments as indicated by the black line in (a) confirms the formation of both Cp* and FeCp* species.

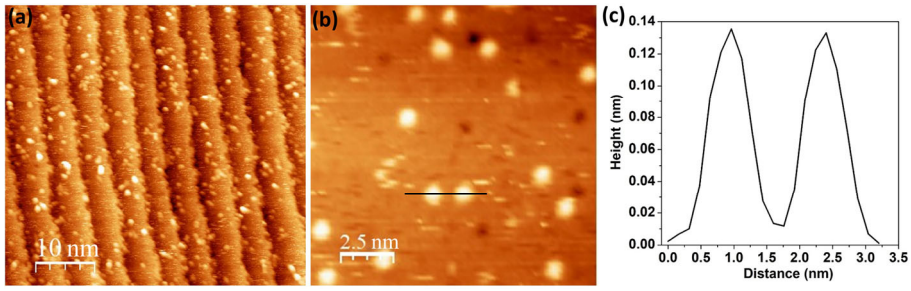

Figure 3 STM images of Pt(111) after exposure to 15 L $FeCp_2$ at 298 K followed by annealing in 1×10^{-6} mbar O_2 at 473 K. Scanning parameters are (a) 0.76 V and 0.32 nA; (b) 0.77 V and 0.33 nA. (c) Line profile across two isolated Fe_1O_x protrusions as indicated by the black line in (b).

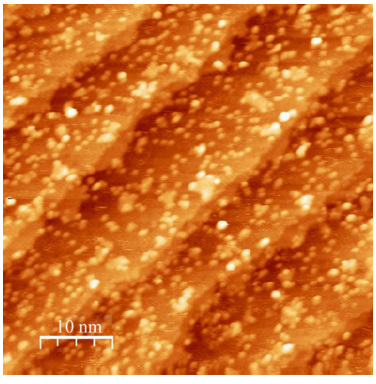

Figure 4 STM image of 45 L $FeCp_2$ deposited on Pt(111) at 298 K followed by annealing in 1×10^{-6} mbar O_2 at 473 K. Scanning parameters are 1.1 V and 0.31 nA.

We investigated the stability of the protrusions towards sintering by increasing the sample temperature in UHV to 673 K. We surprisingly find that although larger nanoparticles are formed, a considerable fraction of the monodispersed iron oxide protrusions still survive after such high temperature treatment (see Fig. S3 in the ESM), distinctly different from the FeO_x film prepared by PVD where triangular FeO_x inslands with above 10 nm size are usually formed after the same annealing treatment [40].

To simulate conventional ALD preparation conditions, we exposed the Pt(111) surface to a saturating dose of 500 L $FeCp_2$. The preparation was investigated using AP-XPS and STM (Fig. 5). After exposure, the surface is covered by a dense network of ferrocene fragments. Observation of the bare Pt(111) surface was not feasible at this coverage, in agreement with previous STM studies of saturated doses of ferrocene on platinum [32]. The Fe 2p spectrum shows a peak at 707.6 eV corresponding to Fe coordinated to a Cp ligand and the Pt(111) surface. The main peak in the C 1s region is positioned at 284.2 eV and can be assigned to carbon atoms in cyclopentadienyl rings [32]. The weak shoulder in the C 1s spectrum (Fig. 5(b), black arrow) at about 286.5 eV is assigned to co-adsorbed CO originating from trace level impurities introduced during the ferrocene exposure.

Annealing the sample in 1×10^{-6} mbar O_2 at 473 K removes the Cp ligands from the surface as confirmed by XPS (Fig. 6(b)). As a consequence, all protrusions in the STM images (Fig. 6(a)) can be assigned to iron oxide species. Small protrusions, associated to isolated iron species, are observed as well as patches of clean Pt areas. However, at this coverage, the surface may also include a small number of iron oxide clusters. The apparent slight difference in dimensions of the isolated iron species may be explained by blunt tip conditions caused by tip–cluster interaction during scanning. The capacity to resolve individual clusters is also influenced by the lateral separation of iron species and the proximity to platinum step edges.

Even though a dose of 500 L $FeCp_2$ is above the saturation dose on Pt(111), regions of exposed Pt(111) can be observed by STM after the O_2 annealing step. This may be rationalized by a combination of recombinative desorption of Cp* and FeCp* adsorbates and oxidation of isolated Cp and Cp coordinated to Fe. The latter process leaves a single Fe_1O_x site at the surface.

Figure 7(a) shows STM results obtained after two ALD cycles of 500 L ferrocene exposure at 298 K and annealing in 1×10^{-6} mbar O_2 at 473 K. The size distribution of the protrusions observed in the STM images is considerably wider than what is found after a single ALD cycle (Fig. 6). The surface is almost entirely covered by nanoclusters suggesting that under these conditions isolated oxidized iron species are minority species. The increase in FeO_x coverage agrees well with the near linear increase in intensity of the Fe 2p peak in the XPS spectrum (Fig. 7(b)), indicating unrestricted continued growth of FeO_x during the second cycle.

The study by Cao et al. reports high activity and selectivity for the PROX reaction using a catalyst comprised of atomically dispersed iron hydroxide $Fe(OH)_x$ sites on platinum nanoparticles [28]. Here, we employed AP-XPS to a related model system to

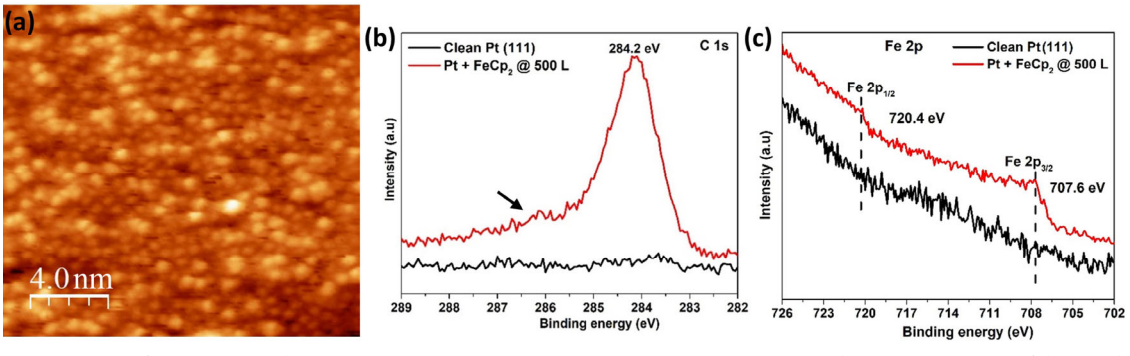

Figure 5 (a) STM image of Pt(111) exposed to 500 L $FeCp_2$ at 298 K. STM scanning parameters are 1.38 V and 0.29 nA. XP spectra of (b) C 1s (hv = 750 eV) and (c) Fe 2p ($h\nu$ = 900 eV) regions collected from the clean Pt(111) surface (black lines) and after adsorption of 500 L $FeCp_2$ (red lines).

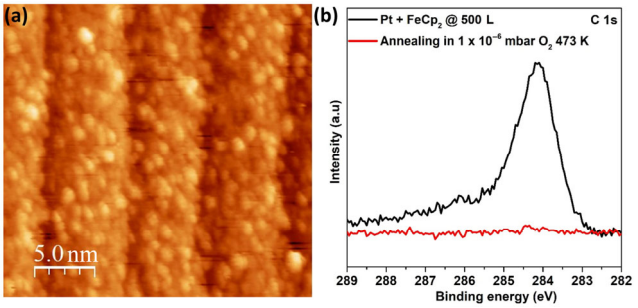

Figure 6 (a) STM image of Pt(111) after exposure to 500 L $FeCp_2$ at 298 K followed by annealing in 1×10^{-6} mbar O_2 at 473 K. Scanning parameters are −0.25 V and 0.29 nA. (b) C 1s ($h\nu$ = 750 eV) XP spectra collected for a 500 L $FeCp_2$ dose before (black) and after (red) O_2 treatment at 1×10^{-6} mbar and 473 K.

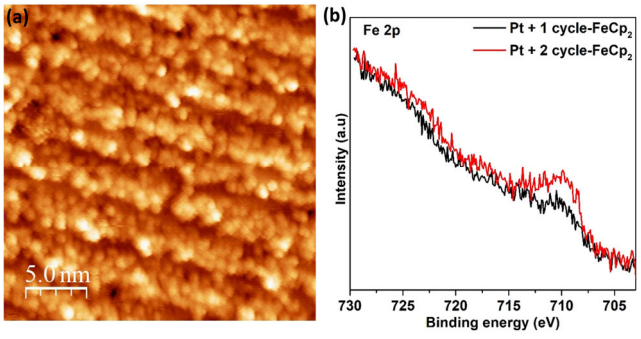

Figure 7 (a) STM image after two complete ALD cycles of 500 L $FeCp_2$ on Pt(111) at 298 K and annealing in 1×10^{-6} mbar O_2 at 473 K. Scanning parameters are 1.5 V and 0.35 nA. (b) Fe 2p ($h\nu$ = 900 eV) XP spectra after one (black) and two (red) ALD cycles.

provide insights into the dynamics of the active sites and reaction mechanism under relevant conditions. The surface properties of two different samples were compared in order to elucidate the role of single hydroxylated iron atoms or nanoclusters as active sites. Figure 8 shows AP-XPS results from a single ALD cycle sample (500 L $FeCp_2$). This sample preparation results in isolated iron species as the dominant surface species, as shown in the STM image of Fig. 6. The single-site iron oxide covered surface was fabricated through exposure to 1 mbar O_2 at 373 K in the ambient pressure cell of the analysis chamber. The main peak of the O 1s spectrum (at 529.3 eV, black curve) is assigned to a combination of oxygen atoms coordinated to Fe and dissociatively adsorbed oxygen on bare patches of the Pt(111) surface. We cannot differentiate these two adsorption sites due to their overlapping binding energies

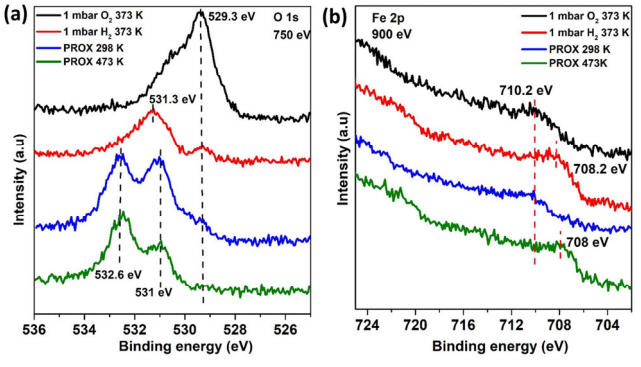

Figure 8 Ambient pressure O 1s and Fe 2p XP spectra from a single ALD cycle/Pt(111) surface. The spectra were collected under sequential treatment of 1 mbar O_2, 1 mbar H_2 and during PROX conditions (H_2:CO:O_2 = 4:2:1, total pressure 1 mbar). Photon energies for the O 1s and the Fe 2p were 750 and 900 eV, respectively.

[41–43]. The distinct shoulder on the high binding energy side can, however, be assigned to hydroxyl species originating from trace levels of water in the O_2 gas stream [43, 44]. This binding energy also corresponds to oxygen atoms linked to a carbon atom (e.g. CO bridge position on Pt(111)); however, no carbon species are observed in the corresponding C 1s spectrum ruling out this interpretation (see Fig. S4 in the ESM). The corresponding Fe 2p spectrum shows a peak at 710.2 eV, a binding energy in the range of what has been reported for Fe^{3+} [40, 45, 46]. The sample was then reduced in 1 mbar H_2 at 373 K (red line in Fig. 8). The intensity of the main O 1s peak at 529.3 eV decreases significantly, while the shoulder at 531.3 eV, previously assigned to hydroxyl groups, increases in intensity. The changes in the O 1s region is interpreted as hydroxylation of oxygen atoms coordinated to Fe in combination with water formation and desorption on the patches with oxygen adsorbed on Pt(111) [47, 48]. The weak O 1s peak at 529.3 eV may tentatively be assigned to a low coverage of iron oxide clusters that cannot be completely hydroxylated under the present conditions. The relative peak intensity (from curve fitting) of the single-site iron hydroxide species and iron oxide cluster is 10 to 1, suggesting that most of the protrusions in Fig. 6 are single-site iron oxide species. Simultaneously, the peak in Fe 2p shifts from 710.2 to 708.2 eV, in the binding energy range corresponding to Fe^{2+} species on Pt(111) [45]. The combined Fe 2p and O 1s results indicate formation of iron hydroxide $Fe_1(OH)_2$, in agreement with what has been reported for single-site iron hydroxide supported on Pt particles [28].

After the reduction treatment, the sample was exposed to conditions relevant for the PROX reaction (gas flow ratios H_2:CO:O_2 = 4:2:1, at 1 mbar total pressure) at increasing temperature. Two distinct peaks at 531.0 and 532.6 eV are observed in the O 1s region at 298 K (blue curve, Fig. 8). These peaks are assigned to bridge and atop site adsorption of CO on the bare Pt(111) surface [41, 49]. The CO adsorption is confirmed by the C 1s spectrum (Fig. S5 in the ESM). The adsorption of CO, especially at bridge sites on Pt(111), confirms the presence of patches of Pt(111) surface not covered by FeO_x, in agreement with the previous STM observations. However, the O 1s peak at 531.0 eV also contains a contribution from Fe coordinated hydroxyl groups. The C 1s intensity ratio between CO atop to bridge sites is found to be 1.6:1 while in O 1s the combined intensity for CO bridge and hydroxyl sites is similar to the intensity contribution from CO atop sites (as shown in Figs. S5–S7 in the ESM). This allows us to deduce the relative contribution of hydroxyls to the 531.0 eV peak to approximately 36%. The weak iron oxide peak at 529.3 eV previously observed during the calcination treatment is still observed, suggesting no change in the state of the low coverage of iron oxide nanoclusters. The Fe 2p peak shifts back to 710.2 eV indicative of formation of a Fe^{3+} state for a majority of the species. This is in agreement with the suggested structure for single site $Fe_1(OH)_3$ supported on Pt nanoclusters [28]. However, the line shape of the spectrum cannot exclude minor contributions from 2+ species, if present, such minority species may tentatively be associated to iron oxide clusters. Taken together, the results show the formation of $Fe_1(OH)_3$ as majority species on the surface. The temperature was then increased to 373 K under the same PROX conditions. The line profiles of the O 1s and the Fe 2p spectra show no large changes (not shown). However, close inspection of the relative intensities shows a 7% loss of the CO bridge species adsorbed on Pt(111) along with 12% loss of the hydroxyl groups coordinated to Fe. This observation is in agreement with what can be expected for preferential oxidation of CO involving OH groups at the

$Fe_1(OH)_3$ sites. When the temperature is increased to 473 K, we observe a reduction in CO bridge peak intensity that corresponds to a 32% loss and a reduction of 26% in the OH coverage compared to the coverages at 298 K. Simultaneously the Fe 2p peak shifts to 708 eV indicating that the iron species are reduced to a predominantly 2+ state [46, 50]. Together the O 1s and Fe 2p observations indicate the formation of a majority of iron species in the form of $Fe_1(OH)_2$. A considerable decrease in the OH XPS intensity for the PROX reaction at 473 K compared to that at 298 K (Fig. 8(a)) suggests a limitation in the oxygen supply necessary for the preferential CO oxidation reaction and regeneration of the catalyst. This observation implies that the competing hydrogen oxidation reaction $2H_2 + O_2 = 2H_2O$ is not negligible at this temperature, in line with the previous work suggesting that the CO selectivity decreases at approximately 380 K on a single-site $Fe_1(OH)_x$/Pt nanoparticle catalyst [28].

Based on the above experimental observations, a reaction mechanism similar to what was originally proposed by Cao et al. for a $Fe_1(OH)_3$/Pt nanoparticle catalyst may be suggested for the present model catalyst system [28]. The rate-limiting step in the catalytic cycle is the initial formation of COOH* species through combination of CO adsorbed on a Pt site and an OH group of the $Fe_1(OH)_3$. This agrees favorably with the by XPS determined chemical state of iron as hydroxylated Fe^{3+} and detection of CO adsorbates on Pt sites at room temperature (Fig. 8). Adsorbed CO blocks the adsorption molecular oxygen on Pt(111) sites under conditions for ambient-pressure PROX reaction [34]. However, molecular oxygen from the gas stream may adsorb and dissociate at the single iron sites forming a $Fe(OH)_2O_2$/Pt(111) intermediate. An oxygen atom from $Fe(OH)_2O_2$/Pt(111) combines with COOH* to form an OH group and CO_2. The catalyst is now in the state $Fe(OH)_3O$/Pt(111). The lone oxygen atom of the catalyst combines with a CO adsorbed on a nearby Pt site to form CO_2, regenerating the catalyst and closing the reaction cycle. In addition, the preferential consumption of bridge CO at 473 K (Fig. 8(a), green line) is also consistent with the proposed mechanism. The CO supply from the gas steam is insufficient to replenish the CO surface coverage at the increased reaction rate for 473 K. The slightly weaker adsorption of bridge CO may lead to a preferential reaction including this site. Minor contributions to the reduction in CO coverage are also expected from the CO oxidation reaction on Pt(111) at 473 K [51].

Figure 9 presents XPS results for a two ALD cycles sample. As shown in the STM results above, this preparation condition results in significant formation of iron oxide nanoclusters and only minor fractions of isolated Fe_1O_x species. Similar to the one ALD cycle experiment, oxidation in 1 mbar O_2 at 473 K results in iron oxide formation in the form of Fe^{3+} (peak at 529.3 eV in the O 1s and 710.1 eV in the Fe 2p). However, reduction under H_2 ambient at 473 K does not result in as significant hydroxylation as in the case for the single ALD cycle preparation (see O 1s and Fe 2p). A control experiment was performed over the one ALD cycle sample by exposure to 1 mbar O_2 at 473 K followed by 1 mbar H_2 at 473 K as shown in Fig. S8 in the ESM. The preparation results in a clear signature of hydroxylation. The observation demonstrates that iron oxide nanoclusters are not readily hydroxylated, in striking contrast to the facile hydroxylation of the single Fe atom species formed in one ALD cycle preparations. The presence of a peak in O 1s at 529.3 eV is in good agreement with the location of the Fe 2p peak at 707.8 eV for iron oxide [45]. The distinct nature of the interaction with hydrogen compared to a single cycle ALD sample is another indication of a different iron oxide structure formed [52]. The observation of CO lines during the H_2 exposure is attributed to trace contaminants from the gas stream. We note that CO adsorption is not detected in one cycle ALD sample under similar H_2 exposure (Fig. 8(a), red line), likely due to effective removal through CO oxidation by the highly active single-site iron hydroxide.

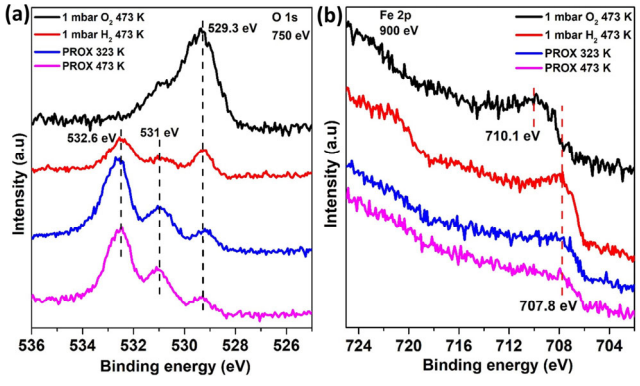

Figure 9 *In-situ* O 1s and Fe 2p XPS spectra on a two ALD cycles sample. The spectra were collected under sequential treatment of 1 mbar O_2, 1 mbar H_2, and PROX conditions. Reaction conditions for PROX: H_2:CO:O_2 = 4:2:1, total pressure 1 mbar. The photon energies for O 1s and Fe 2p were 750 and 900 eV, respectively.

Upon introduction of PROX gas into the chamber the peaks at 531 and 532.6 eV, corresponding to CO bridge and CO atop adsorption, grow in intensity. However, the relative intensity between CO bridge and CO atop is different compared with what is observed for the single ALD cycle of iron oxide. The relative ratio in C 1s between CO atop and bridge sites is 1.6:1 for the one ALD cycle sample (see Fig. S7 in the ESM) and it is 2.7:1 for the two ALD cycles sample (see Fig. S10 in the ESM), which is consistent with the anticipated increased site blockage at this high coverage of iron oxide clusters as shown by the STM results (Fig. 7). No changes in the iron oxidation state, on the Fe 2p spectrum, are observed during exposure to the PROX reaction gas. This shows that the iron oxide nanoparticles, the majority species for this preparation, are not readily re-oxidized into a 3+ state, as is the case for single-site iron oxide. The observation of a stable chemical Fe^{2+} state is in line with the results from studies of FeO_x islands on Pt(111) where it has been reported that the presence of CO or H_2 in the PROX gas mixture stabilizes the iron species against oxidation to Fe^{3+} [34]. This may suggest that a similar reaction mechanism is relevant in the present system, in which oxygen gas adsorbs and dissociates at the interfaces of FeO-Pt(111) and then reacts with nearby CO adsorbed on the Pt substrate [40]. The results from curve fitting (Fig. S9 in the ESM) show that the intensities of CO bridge and CO atop as well as iron oxide coverage do not change as the temperature is increased to 473 K, suggesting that CO cannot be oxidized under these conditions.

4 Conclusions

We have successfully synthesized an atomically dispersed $Fe_1(OH)_x$ (and Fe_1O_x) inverse model catalyst supported on a Pt(111) surface by taking advantage of the steric hindrance of the $FeCp_2$ precursor. The synthesis of single-site Fe_1O_x species was investigated in detail by STM for several $FeCp_2$ doses (15, 45 and 500 L). We conducted *in-situ* AP-XPS studies of the surface to monitor the dynamic changes of this model catalyst in the presence of reactive gas streams. XPS results suggest that the Fe_1O_x motifs are transformed into $Fe_1(OH)_2$ by reduction and hydroxylation in 1 mbar H_2 at 373 K. An oxidation process proceeds through additional hydroxylation and results in the formation of $Fe_1(OH)_3$ species under PROX reaction gas

at room temperature. For synthesized iron oxide nanoparticles, no obvious hydroxylation is observed under H_2 ambient and the nanoparticles could not be re-oxidized under PROX conditions. By monitoring the CO surface species, we show preferential oxidation of CO involving the OH groups at the $Fe_1(OH)_3$ sites while no obvious CO oxidation is detected over the iron oxide nanoparticles. This observation is fundamental to the understanding of the PROX reaction in this system, as it shows that the flexibility of the iron oxidation state facilitates the CO oxidation. The results highlight striking differences in chemical properties between iron oxide in the form of single-sites and nanoparticles. In addition, the described ALD method may provide a new strategy to precisely synthesize inverse model catalysts of atomically dispersed oxides to nanoparticles and may easily be extended to other model systems.

Acknowledgements

This work was funded by the Swedish Research Council (VR), the Knut och Alice Wallenbergs stiftelse, and the STINT Joint China-Sweden Mobility program. H. T. acknowledges the financial support from the Ragnar Holm foundation, C. W. the financial support from Trygger's foundation. The MAX IV staff are gratefully acknowledged for their support during beamtimes.

Funding note: Open access funding provided by Royal Institute of Technology.

Electronic Supplementary Material: Supplementary material (STM images of the clean Pt(111) surface and the same surface after $FeCp_2$ adsorption and details of the XPS fitting results) is available in the online version of this article at https://doi.org/10.1007/s12274-021-3551-4.

Reference

[1] Fu, Q.; Yang, F.; Bao, X. H. Interface-confined oxide nanostructures for catalytic oxidation reactions. *Acc. Chem. Res.* **2013**, *46*, 1692–1701.

[2] Haruta, M. Gold as a novel catalyst in the 21st century: Preparation, working mechanism and applications. *Gold Bull.* **2004**, *37*, 27–36.

[3] Green, I. X.; Tang, W. J.; Neurock, M.; Yates, J. T. Jr. Spectroscopic observation of dual catalytic sites during oxidation of CO on a Au/TiO_2 catalyst. *Science* **2011**, *333*, 736–739.

[4] Wang, C. L.; Wang, H. W.; Yao, Q.; Yan, H.; Li, J. J.; Lu, J. L. Precisely applying TiO_2 overcoat on supported Au catalysts using atomic layer deposition for understanding the reaction mechanism and improved activity in CO oxidation. *J. Phys. Chem. C* **2016**, *120*, 478–486.

[5] Chen, G. X.; Zhao, Y.; Fu, G.; Duchesne, P. N.; Gu, L.; Zheng, Y. P.; Weng, X. F.; Chen, M. S.; Zhang, P.; Pao, C. W. et al. Interfacial effects in iron-nickel hydroxide–platinum nanoparticles enhance catalytic oxidation. *Science* **2014**, *344*, 495–499.

[6] Graciani, J.; Mudiyanselage, K.; Xu, F.; Baber, A. E.; Evans, J.; Senanayake, S. D.; Stacchiola, D. J.; Liu, P.; Hrbek, J.; Sanz, J. F. et al. Highly active copper-ceria and copper-ceria-titania catalysts for methanol synthesis from CO_2. *Science* **2014**, *345*, 546–550.

[7] Mudiyanselage, K.; Senanayake, S. D.; Feria, L.; Kundu, S.; Baber, A. E.; Graciani, J.; Vidal, A. B.; Agnoli, S.; Evans, J.; Chang, R. et al. Importance of the metal–oxide interface in catalysis: *In situ* studies of the water–gas shift reaction by ambient-pressure X-ray photoelectron spectroscopy. *Angew. Chem., Int. Ed.* **2013**, *52*, 5101–5105.

[8] Freund, H. J.; Pacchioni, G. Oxide ultra-thin films on metals: New materials for the design of supported metal catalysts. *Chem. Soc. Rev.* **2008**, *37*, 2224–2242.

[9] Pan, Q. S.; Weng, X. F.; Chen, M. S.; Giordano, L.; Pacchioni, G.; Noguera, C.; Goniakowski, J.; Shaikhutdinov, S.; Freund, H. J. Enhanced CO oxidation on the oxide/metal interface: From ultra-high vacuum to near-atmospheric pressures. *ChemCatChem* **2015**, *7*, 2620–2627.

[10] Lin, J.; Qiao, B. T.; Liu, J. Y.; Huang, Y. Q.; Wang, A. Q.; Li, L.; Zhang, W. S.; Allard, L. F.; Wang, X. D.; Zhang, T. Design of a highly active $Ir/Fe(OH)_x$ catalyst: Versatile application of Pt-group metals for the preferential oxidation of carbon monoxide. *Angew. Chem., Int. Ed.* **2012**, *124*, 2974–2978.

[11] Wang, H. W.; Gu, X. K.; Zheng, X. S.; Pan, H. B.; Zhu, J. F.; Chen, S.; Cao, L. N.; Li, W. X.; Lu, J. L. Disentangling the size-dependent geometric and electronic effects of palladium nanocatalysts beyond selectivity. *Sci. Adv.* **2019**, *5*, eaat6413.

[12] Maeda, Y.; Iizuka, Y.; Kohyama, M. Generation of oxygen vacancies at a Au/TiO_2 perimeter interface during CO oxidation detected by *in situ* electrical conductance measurement. *J. Am. Chem. Soc.* **2013**, *135*, 906–909.

[13] Pan, Q.; Li, L.; Shaikhutdinov, S.; Fujimori, Y.; Hollerer, M.; Sterrer, M.; Freund, H. J. Model systems in heterogeneous catalysis: Towards the design and understanding of structure and electronic properties. *Faraday Discuss.* **2018**, *208*, 307–323.

[14] Trotochaud, L.; Head, A. R.; Pletincx, S.; Karslıoğlu, O.; Yu, Y.; Waldner, A.; Kyhl, L.; Hauffman, T.; Terryn, H.; Eichhorn, B. et al. Water adsorption and dissociation on polycrystalline copper oxides: Effects of environmental contamination and experimental protocol. *J. Phys. Chem. B* **2018**, *122*, 1000–1008.

[15] Freund, H. J. The surface science of catalysis and more, using ultrathin oxide films as templates: a perspective. *J. Am. Chem. Soc.* **2016**, *138*, 8985–8996.

[16] Therrien, A. J.; Hensley, A. J. R.; Marcinkowski, M. D.; Zhang, R. Q.; Lucci, F. R.; Coughlin, B.; Schilling, A. C.; McEwen, J. S.; Sykes, E. C. H. An atomic-scale view of single-site Pt catalysis for low-temperature CO oxidation. *Nat. Catal.* **2018**, *1*, 192.

[17] Dou, J.; Sun, Z. C.; Opalade, A. A.; Wang, N.; Fu, W. S.; Tao, F. *Operando* chemistry of catalyst surfaces during catalysis. *Chem. Soc. Rev.* **2017**, *46*, 2001–2027.

[18] Sauer, J.; Freund, H. J. Models in catalysis. *Catal. Lett.* **2015**, *145*, 109–125.

[19] Leisenberger, F. P.; Surnev, S.; Koller, G.; Ramsey, M. G.; Netzer, F. P. Probing the metal sites of a vanadium oxide–Pd(111) 'inverse catalyst': Adsorption of CO. *Surf. Sci.* **2000**, *444*, 211–220.

[20] Schoiswohl, J.; Surnev, S.; Netzer, F. P. Reactions on inverse model catalyst surfaces: Atomic views by STM. *Top. Catal.* **2005**, *36*, 91–105.

[21] Senanayake, S. D.; Stacchiola, D.; Rodriguez, J. A. Unique properties of ceria nanoparticles supported on metals: Novel inverse ceria/copper catalysts for CO oxidation and the water-gas shift reaction. *Acc. Chem. Res.* **2013**, *46*, 1702–1711.

[22] Fujitani, T.; Nakamura, I. Mechanism and active sites of the oxidation of CO over Au/TiO_2. *Angew. Chem., Int. Ed.* **2011**, *50*, 10144–10147.

[23] Zhang, J.; Medlin, J. W. Catalyst design using an inverse strategy: From mechanistic studies on inverted model catalysts to applications of oxide-coated metal nanoparticles. *Surf. Sci. Rep.* **2018**, *73*, 117–152.

[24] Kudernatsch, W.; Peng, G. W.; Zeuthen, H.; Bai, Y. H.; Merte, L. R.; Lammich, L.; Besenbacher, F.; Mavrikakis, M.; Wendt, S. Direct visualization of catalytically active sites at the FeO–Pt(111) interface. *ACS Nano* **2015**, *9*, 7804–7814.

[25] Liu, Y.; Yang, F.; Zhang, Y.; Xiao, J. P.; Yu, L.; Liu, Q. F.; Ning, Y. X.; Zhou, Z. W.; Chen, H.; Huang, W. G. et al. Enhanced oxidation resistance of active nanostructures via dynamic size effect. *Nat. Commun*. **2017**, *8*, 14459.
[26] Sun, Y. N.; Giordano, L.; Goniakowski, J.; Lewandowski, M.; Qin, Z. H.; Noguera, C.; Shaikhutdinov, S.; Pacchioni, G.; Freund, H. J. The interplay between structure and CO oxidation catalysis on metal-supported ultrathin oxide films. *Angew. Chem., Int. Ed*. **2010**, *49*, 4418–4421.
[27] Ritter, M.; Ranke, W.; Weiss, W. Growth and structure of ultrathin FeO films on Pt(111) studied by STM and LEED. *Phys. Rev. B* **1998**, *57*, 7240.
[28] Cao, L.; Liu, W.; Luo, Q. Q.; Yin, R. T.; Wang, B.; Weissenrieder, J.; Soldemo, M.; Yan, H.; Lin, Y.; Sun, Z. H. et al. Atomically dispersed iron hydroxide anchored on Pt for preferential oxidation of CO in H_2. *Nature* **2019**, *565*, 631.
[29] Lu, J. L.; Elam, J. W.; Stair, P. C. Synthesis and stabilization of supported metal catalysts by atomic layer deposition. *Acc. Chem. Res*. **2013**, *46*, 1806–1815.
[30] Braun, K. F.; Iancu, V.; Pertaya, N.; Rieder, K. H.; Hla, S. W. Decompositional incommensurate growth of ferrocene molecules on a Au(111) surface. *Phys. Rev. Lett*. **2006**, *96*, 246102.
[31] Dunitz, J.; Orgel, L.; Rich, A. The crystal structure of ferrocene. *Acta Cryst*. **1956**, *9*, 373–375.
[32] Paul, R.; Reifenberger, R. G.; Fisher, T. S.; Zemlyanov, D. Y. Atomic layer deposition of FeO on Pt(111) by ferrocene adsorption and oxidation. *Chem. Mater*. **2015**, *27*, 5915–5924.
[33] Lu, J. L.; Fu, B. S.; Kung, M. C.; Xiao, G. M.; Elam, J. W.; Kung, H. H.; Stair, P. C. Coking-and sintering-resistant palladium catalysts achieved through atomic layer deposition. *Science* **2012**, *335*, 1205–1208.
[34] Chen, H.; Liu, Y.; Yang, F.; Wei, M. M.; Zhao, X. F.; Ning, Y. X.; Liu, Q. F.; Zhang, Y.; Fu, Q.; Bao, X. H. Active phase of FeO_x/Pt catalysts in low-temperature CO oxidation and preferential oxidation of CO reaction. *J. Phys. Chem. C* **2017**, *121*, 10398–10405.
[35] Shaikhutdinov, S.; Ritter, M.; Weiss, W. Hexagonal heterolayers on a square lattice: A combined STM and LEED study of FeO(111) on Pt(100). *Phys. Rev. B* **2000**, *62*, 7535.
[36] Merte, L. R.; Shipilin, M.; Ataran, S.; Blomberg, S.; Zhang, C.; Mikkelsen, A.; Gustafson, J.; Lundgren, E. Growth of ultrathin iron oxide films on Ag(100). *J. Phys. Chem. C* **2015**, *119*, 2572–2582.
[37] Wang, W.; Zhang, H.; Wang, W. H.; Zhao, A. D.; Wang, B.; Hou, J. G. Observation of water dissociation on nanometer-sized FeO islands grown on Pt(1 1 1). *Chem. Phys. Lett*. **2010**, *500*, 76–81.
[38] Zhou, X.; Shen, Q.; Yuan, K. D.; Yang, W. S.; Chen, Q. W.; Geng, Z. H.; Zhang, J. L.; Shao, X.; Chen, W.; Xu, G. Q. et al. Unraveling charge state of supported Au single-atoms during CO oxidation. *J. Am. Chem. Soc*. **2018**, *140*, 554–557.
[39] Gumbsch, A.; Barcaro, G.; Ramsey, M. G.; Surnev, S.; Fortunelli, A.; Netzer, F. P. Kondo effect of cobalt adatoms on nanostructured Cu-O surfaces: Scanning tunneling spectroscopy experiments and first-principles calculations. *Phys. Rev. B* **2010**, *81*, 165420.
[40] Fu, Q.; Li, W. X.; Yao, Y. X.; Liu, H. Y.; Su, H. Y.; Ma, D.; Gu, X. K.; Chen, L. M.; Wang, Z.; Zhang, H. et al. Interface-confined ferrous centers for catalytic oxidation. *Science* **2010**, *328*, 1141–1144.
[41] Knudsen, J.; Andersen, J. N.; Schnadt, J. A versatile instrument for ambient pressure X-ray photoelectron spectroscopy: The Lund cell approach. *Surf. Sci*. **2016**, *646*, 160–169.
[42] Björneholm, O.; Nilsson, A.; Tillborg, H.; Bennich, P.; Sandell, A.; Hernnäs, B.; Puglia, C.; Mårtensson, N. Overlayer structure from adsorbate and substrate core level binding energy shifts: CO, CCH_3 and O on Pt(111). *Surf. Sci*. **1994**, *315*, L983–L989.
[43] Ringleb, F.; Fujimori, Y.; Wang, H. F.; Ariga, H.; Carrasco, E.; Sterrer, M.; Freund, H. J.; Giordano, L.; Pacchioni, G.; Goniakowski, J. Interaction of water with FeO(111)/Pt(111): environmental effects and influence of oxygen. *J. Phys. Chem. C* **2011**, *115*, 19328–19335.
[44] Wei, M. M.; Fu, Q.; Dong, A. Y.; Wang, Z. J.; Bao, X. H. Coverage and substrate effects on the structural change of FeO_x nanostructures supported on Pt. *Top. Catal*. **2014**, *57*, 890–898.
[45] Kaya, S.; Ogasawara, H.; Nilsson, A. Determination of the surface electronic structure of Fe_3O_4(1 1 1) by soft X-ray spectroscopy. *Catal. Today*. **2015**, *240*, 184–189.
[46] Graat, P. C. J.; Somers, M. A. J. Simultaneous determination of composition and thickness of thin iron-oxide films from XPS Fe 2p spectra. *Appl. Surf. Sci*. **1996**, *100–101*, 36–40.
[47] Gland, J. L.; Fisher, G. B.; Kollin, E. B. The hydrogen-oxygen reaction over the Pt(111) surface: Transient titration of adsorbed oxygen with hydrogen. *J. Catal*. **1982**, *77*, 263–278.
[48] Fisher, G. B.; Sexton, B. A. Identification of an adsorbed hydroxyl species on the Pt(111) surface. *Phys. Rev. Lett*. **1980**, *44*, 683.
[49] Calderón, S. K.; Grabau, M.; Óvári, L.; Kress, B.; Steinrück, H. P.; Papp, C. CO oxidation on Pt(111) at near ambient pressures. *J. Chem. Phys*. **2016**, *144*, 044706.
[50] Descostes, M.; Mercier, F.; Thromat, N.; Beaucaire, C.; Gautier-Soyer, M. Use of XPS in the determination of chemical environment and oxidation state of iron and sulfur samples: Constitution of a data basis in binding energies for Fe and S reference compounds and applications to the evidence of surface species of an oxidized pyrite in a carbonate medium. *Appl. Surf. Sci*. **2000**, *165*, 288–302.
[51] Schnadt, J.; Knudsen, J.; Andersen, J. N.; Siegbahn, H.; Pietzsch, A.; Hennies, F.; Johansson, N.; Mårtensson, N.; Öhrwall, G.; Bahr, S. et al. The new ambient-pressure X-ray photoelectron spectroscopy instrument at MAX-lab. *J. Synchrotron Rad*. **2012**, *19*, 701–704.
[52] Fu, Q.; Yao, Y. X.; Guo, X. G.; Wei, M. M.; Ning, Y. X.; Liu, H. Y.; Yang, F.; Liu, Z.; Bao, X. H. Reversible structural transformation of FeO_x nanostructures on Pt under cycling redox conditions and its effect on oxidation catalysis. *Phys. Chem. Chem. Phys*. **2013**, *15*, 14708–14714.